

Discovery of a 300-day Period from the Enshrouded Massive Binary NaSt1 (WR 122), a Product of Binary Interaction

RYAN M. LAU,¹ SAMAPORN TINYANONT,² MATTHEW J. HANKINS,³ MICHAEL C. B. ASHLEY,⁴ KISHALAY DE,⁵
ALEXEI V. FILIPPENKO,^{6,7} LYNNE A. HILLENBRAND,⁵ MANSI M. KASLIWAL,⁵ JON C. MAUERHAN,⁸
ANTHONY F. J. MOFFAT,⁹ ANNA M. MOORE,¹⁰ NATHAN SMITH,¹¹ JAMIE SOON,¹⁰ ROBERTO SORIA,¹²
TONY TRAVOUILLON,¹⁰ KAREL A. VAN DER HUCHT,¹³ PEREDUR M. WILLIAMS,¹⁴ AND WEIKANG ZHENG⁶

¹*Institute of Space & Astronautical Science, Japan Aerospace Exploration Agency, 3-1-1 Yoshinodai, Chuo-ku, Sagami-hara, Kanagawa 252-5210, Japan*

²*Department of Astronomy and Astrophysics, University of California, 1156 High St., Santa Cruz, CA 95064, USA*

³*Department of Physical Sciences, Arkansas Tech University, 1701 N. Boulder Avenue, Russellville, AR 72801, USA*

⁴*School of Physics, University of New South Wales, Sydney NSW 2052, Australia*

⁵*Division of Physics, Mathematics, and Astronomy, California Institute of Technology, Pasadena, CA 91125, USA*

⁶*Department of Astronomy, University of California, Berkeley, CA 94720-3411, USA*

⁷*Miller Institute for Basic Research in Science, University of California, Berkeley, CA 94720, USA*

⁸*The Aerospace Corporation, 2310 E. El Segundo Boulevard, El Segundo, CA 90245, USA*

⁹*Département de Physique, Université de Montréal, C.P. 6128, succ. centre-ville, Montréal (Qc) H3C 3J7, Canada; and Centre de Recherche en Astrophysique du Québec, Canada*

¹⁰*Research School of Astronomy and Astrophysics, Australian National University, Canberra, ACT 2611, Australia*

¹¹*University of Arizona, Steward Observatory, 933 N. Cherry Avenue, Tucson, AZ 85721, USA*

¹²*National Astronomical Observatories, Chinese Academy of Sciences, Beijing 100012, People's Republic of China*

¹³*SRON Netherlands Institute for Space Research Sorbonnelaan 2, NL-3584CA Utrecht, the Netherlands*

¹⁴*Institute for Astronomy, University of Edinburgh, Royal Observatory, Edinburgh EH9 3HJ, UK*

Submitted to AAS Journals

ABSTRACT

We present optical and infrared (IR) light curves of the enshrouded massive binary NaSt1 (WR 122) with observations from Palomar Gattini-IR (PGIR), the Zwicky Transient Facility (ZTF), the Katzman Automatic Imaging Telescope (KAIT), and the All-Sky Automated Survey for Supernovae (ASAS-SN). The optical and IR light curves span between 2014 July and 2020 Oct., revealing periodic, sinusoidal variability from NaSt1 with a $P = 305.2 \pm 1.0$ d period. We also present historical IR light curves taken between 1983 July and 1989 May that also indicate NaSt1 exhibits long-term IR variability on timescales of \sim decades. Fixed-period sinusoidal fits to the recent optical and IR light curves show that amplitude of NaSt1's variability is different at different wavelengths and also reveal significant phase offsets of ~ 18 d between the ZTF r and PGIR J light curves. We interpret the ~ 300 d period of the observed variability as the orbital period of a binary system in NaSt1. Assuming a circular orbit and adopting a range of combined stellar mass values in the range 20–100 M_{\odot} in NaSt1, we estimate orbital separations of ~ 2 –4 au. We suggest that the sinusoidal photometric variability of NaSt1 may arise from variations in the line-of-sight optical depth toward circumstellar optical/IR emitting regions throughout its orbit due to colliding-wind dust formation. We provide an interpretation on the nature of NaSt1 and speculate that the mass-transfer process may have been triggered by Roche-lobe overflow (RLOF) during an eruptive phase of a Ofpe/WN9 star. Lastly, we claim that NaSt1 ceased RLOF mass transfer $\lesssim 3400$ yr ago.

Keywords: massive stars — interacting binary stars — Wolf-Rayet stars — light curves — circumstellar dust

1. INTRODUCTION

Almost all massive stars have a close binary companion ($P \lesssim 5000$ d), implying that binary interaction is common in massive stars (Sana et al. 2012; Moe & Di Stefano 2017). The ubiquity of binary interactions such as mass transfer has challenged our understanding of massive-star evolution and notably diverges from the theoretical framework of single-star evolution (e.g., Heger et al. 2003; Groh et al. 2013). Binary interaction can influence mass loss and enable additional massive-star evolutionary pathways beyond the single-star evolution framework (Smith 2014). For example, Roche-lobe overflow (RLOF) is a critical binary mass-transfer processes that can strip the hydrogen envelope of a massive star and lead to the emergence of a helium-rich Wolf-Rayet (WR) star (De Marco & Izzard 2017; Götzberg et al. 2018).

The WR phase is an important evolved stage of a massive star that precedes its end-of-life explosion as a Type Ib/c supernova (SN) or direct collapse to a black hole (Heger et al. 2003; Smith et al. 2011a; Sukhbold et al. 2016). WR binaries may therefore precede the formation of binary black holes and are potential progenitors of black hole mergers (e.g., Belczynski et al. 2016). Populations of stripped-envelope WR stars can also have a profound impact on the ionization of the interstellar medium (ISM) of their host galaxies as well as the intergalactic medium (IGM) beyond (Sander & Vink 2020; Götzberg et al. 2020). WR star dust formation, which has been observed in colliding-winds from carbon-rich WR (WC) stars with OB-star binary companions (e.g., Williams et al. 1987; Tuthill et al. 1999), may also significantly contribute to dust abundances in the ISM of their host galaxies (Lau et al. 2020a).

Understanding the underlying physics that drives the evolution to this stripped-envelope WR phase is therefore of great importance. However, owing to the relatively short timescales associated with the RLOF mass-transfer process, there is a dearth of known massive binary systems for investigating this critical transitional phase. One of the most well-known interacting massive binary systems that is currently undergoing RLOF mass transfer is RY Scuti, which is surrounded by a circumstellar nebula of dust and ionized gas (Gehrz et al. 1995; Grundstrom et al. 2007; Smith et al. 2011b).

The enigmatic NaSt1 system was initially classified as a WR star (known as LS IV +00 5 and WR 122; Nassau & Stephenson 1963; van der Hucht et al. 1981; Massey

& Conti 1983) but had its true nature called into question as a result of high spectral resolution observations by Crowther & Smith (1999). It is now thought to host a stripped-envelope WR star emerging from a RLOF mass-transfer phase with a binary companion (Mauerhan et al. 2015). NaSt1 therefore presents a rare opportunity to investigate this transitional phase, particularly given its relatively nearby distance of $3.03^{+0.60}_{-0.45}$ kpc (Rate & Crowther 2020). An important diagnostic of mass transfer via RLOF are the orbital and stellar properties of the central binary; however, these properties remain largely unknown for NaSt1. The presence of a binary system in NaSt1 was inferred from its surrounding extended ($\sim 7''$) spiral-shaped, nitrogen-rich nebula that is thought to originate from nonconservative mass transfer in the central system (Mauerhan et al. 2015). Mauerhan et al. (2015) also showed that NaSt1 exhibits X-ray emission consistent with colliding-wind WR binaries.

NaSt1 possesses an interesting combination of characteristics that are important for understanding the nature of its binary components. Optical and near-infrared (IR) spectroscopy by Crowther & Smith (1999) showed no obvious stellar lines but revealed narrow nebular emission features consistent with fully CNO-processed material that more closely resembles the chemistry of a nitrogen-rich WR star (WN) rather than a red supergiant (RSG) or an H-rich luminous blue variable (LBV). The unusual chemical composition of NaSt1's nebula has notably drawn comparisons to η Car and its surrounding N-rich nebula (Smith & Morse 2004). High-excitation emission lines from NaSt1 also indicated that the ionizing source of its nebula must possess an effective temperature $\gtrsim 30,000$ K, which is also consistent with the presence of a WR star. Classical WR stars, however, are characterized by broad, full width at half-maximum intensity (FWHM) $\gtrsim 1000$ km s $^{-1}$, emission features that are notably absent from NaSt1's spectrum. Interestingly, many of the strong emission lines from NaSt1 exhibit double-peaked profiles separated by tens of km s $^{-1}$, which may originate from a circumstellar or circumbinary disk that could be obscuring or outshining WR emission features (Mauerhan et al. 2015). NaSt1 is also heavily reddened ($A_V \approx 6.5$ mag; Crowther & Smith 1999) from interstellar and/or circumstellar material. Strong thermal-IR emission from NaSt1 indicated the presence of circumstellar dust that either formed recently or is currently ongoing (Rajagopal et al. 2007).

In this work, we present the discovery of periodic photometric variability from NaSt1 with data from optical and near-IR imaging surveys. These results confirm the binary nature of NaSt1 and reveal new insights for understanding its orbital properties and binary mass-transfer process. This work also presents some of the first science results from the recently commissioned near-IR imaging survey Palomar Gattini-IR (PGIR; Moore & Kasliwal 2019; De et al. 2020a).

2. OBSERVATIONS AND ARCHIVAL DATA

2.1. Gattini-IR *J*-band Photometry

PGIR is a wide-field, time-domain imaging survey located at Palomar Observatory. It utilizes a 30 cm telescope and *J*-band filter similar to the 2MASS *J* filter with a central wavelength of $\lambda_c = 1.235 \mu\text{m}$ and an effective filter bandwidth of $\Delta\lambda = 0.1624 \mu\text{m}$. PGIR achieves a $4.96^\circ \times 4.96^\circ$ field of view (FoV) with its $2\text{k} \times 2\text{k}$ HAWAII-2RG detector and a scale of $8''.7 \text{ pixel}^{-1}$. The entire sky visible from Palomar is imaged by PGIR every ~ 2 nights down to a 5σ detection limit of 14.8 Vega mag¹. The PGIR image processing and photometric calibration are described by De et al. (2020a). The *J*-band saturation limit of PGIR was initially ~ 8.5 mag, but has been subsequently improved to $J \approx 6$ mag after implementing a new readout mode described by De et al. (2020b).

NaSt1, which is located at $\alpha(\text{J2000}) = 18^{\text{h}}52^{\text{m}}17.55^{\text{s}}$ and $\delta(\text{J2000}) = +00^\circ59'44''.3$ (Gaia Collaboration 2018), was well-covered by PGIR imaging fields. In order to investigate the *J*-band variability of NaSt1, forced aperture photometry was performed at its coordinates using a 3-resampled-pixel radius ($\sim 13''$) aperture in PGIR images taken between 2018 Nov. and 2020 Oct. Importantly, source confusion is not an issue since NaSt1 is > 3.8 mag brighter in *J* than all objects within $15''$ of its coordinates (Cutri et al. 2003). Photometry from PGIR and all other platforms included in this work are provided in Table 1.

2.2. KAIT Optical Photometry

Optical *BVRI* photometry of NaSt1 was obtained with the robotic 0.76 m Katzman Automatic Imaging Telescope (KAIT; Filippenko et al. 2001) at Lick Observatory. Additional *Clear*-band (close to the *R* band; see Li et al. 2003) images were also obtained with KAIT. A series of 66 imaging observations of NaSt1 was performed with KAIT between 2014 July and 2015 Nov.

The KAIT observing frequency of NaSt1 ranged from a few days to a few weeks when visible.

All images were reduced using a custom pipeline (Ganeshalingam et al. 2010; Stahl et al. 2019). Point-spread-function (PSF) photometry was then obtained using DAOPHOT (Stetson 1987) from the IDL Astronomy User’s Library². Several nearby stars were chosen from the Pan-STARRS1³ catalog for calibration. Their magnitudes were first transformed into Landolt magnitudes (Landolt 1992) using the empirical prescription presented by Tonry et al. (2012) and then transformed to the KAIT natural system.

Apparent magnitudes were all measured in the KAIT4 natural system. The final results were transformed to the standard system using local calibrators and color terms for KAIT4 as given in Table 4 of Ganeshalingam et al. (2010), except for KAIT *Clear*-band data, where no reliable color term is measured owing to the broad response function. We therefore present the *Clear* magnitude relative to the reference stars in Landolt *R* magnitude, which is essentially in the KAIT natural system.

2.3. BASS Mid-IR Spectroscopy

Mid-IR observations of NaSt1 were made using The Broadband Array Spectrograph System (BASS) sensor (Hackwell et al. 1990) at the 3.6 m Advanced Electro-Optical System (AEOS) telescope on Haleakela, HI, on 2017 Oct. 23, 2018 May 13, 2019 Apr. 6, and 2019 Aug 24 (UT dates are used throughout this paper). AEOS utilizes a chopping secondary mirror, run at 7 Hz for rapid sampling of the background. While observing, a chop-and-nod strategy was used with a chop throw of $\sim 11''$ and a telescope nod of the same distance between exposures. 30 s integrations were obtained per nod position, and 12–26 samples were obtained for each of the AEOS observations (6–13 min total integration).

An off-axis visible-wavelength CCD was used for guiding to keep the source centered in the $4.2''$ instrument aperture during exposures. The resolving power of BASS is 30–125 across a 3–13 μm bandpass. Flux calibration was obtained via observations of the standard star α Lyr (Vega) at an airmass similar to that of the NaSt1 observations. Wavelength calibration of each BASS channel was performed in the lab using a monochromator, and either checked on-sky with observations of a strong mid-IR emission-line source (planetary nebula NGC 7027) or in the dome using a black-body source (hot plate) measured at two temperatures (40°C and 60°C) and attenuated by films of polystyrene

¹ All magnitudes provided in this work are in the Vega magnitude system.

² <http://idlastro.gsfc.nasa.gov/>

³ <http://archive.stsci.edu/panstarrs/search.php>

Table 1. KAIT, ASAS-SN, ZTF, and Gattini-IR Photometry of NaSt1

MJD	<i>B</i> (KAIT)	<i>V</i> (ASAS-SN)	<i>V</i> (KAIT)	<i>g</i> (ZTF)	<i>r</i> (ZTF)	<i>R</i> (KAIT)	<i>I</i> (KAIT)	<i>J</i> (Gattini)
56818.446	16.21 ± 0.04	− ± −	14.38 ± 0.02	− ± −	− ± −	12.82 ± 0.03	12.29 ± 0.03	− ± −
56821.406	16.23 ± 0.06	− ± −	14.39 ± 0.02	− ± −	− ± −	12.82 ± 0.03	12.29 ± 0.03	− ± −
56824.434	16.22 ± 0.07	− ± −	14.38 ± 0.02	− ± −	− ± −	12.81 ± 0.03	12.30 ± 0.03	− ± −
56826.437	16.18 ± 0.04	− ± −	14.38 ± 0.02	− ± −	− ± −	12.80 ± 0.03	12.27 ± 0.03	− ± −
...
...

NOTE—*BgVrRIJ*-band photometry from KAIT, ASAS-SN, ZTF, and Gattini-IR. All magnitudes are given in the Vega system, and uncertainties are 1σ . A full version of this table (with the KAIT *Clear* photometry) is available electronically.

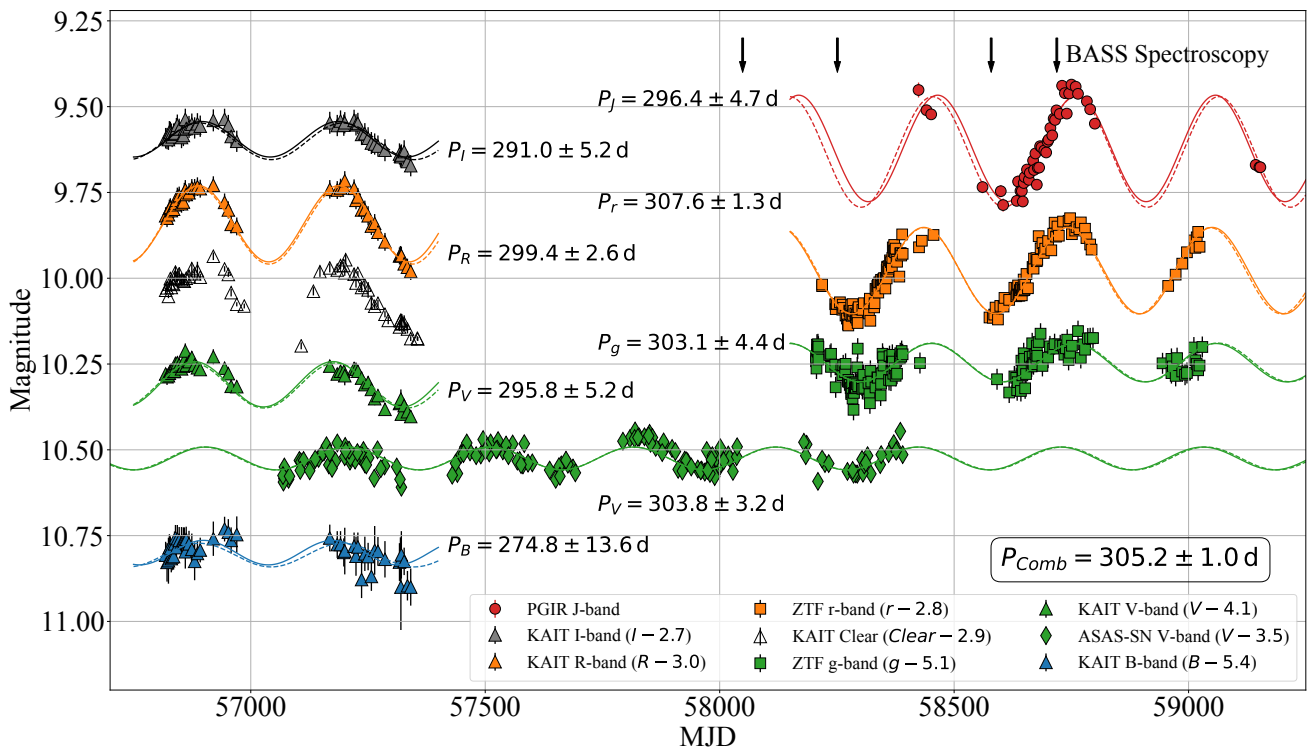


Figure 1. Optical and near-IR light curves of NaSt1 from KAIT (*BVRI* + *Clear*), ASAS-SN (*V*), ZTF (*gr*), and PGIR (*J*) taken between 2014 July and 2020 Oct. The light-curve plot is overlaid with individual-filter (solid line) and fixed-period (dashed line) sinusoidal fits, where the fixed-period fits utilize the 305.2 d period derived from the combined light-curve fit. The individual-filter fit periods (in days) are overlaid on the plot next to their respective light curve. Dates of the four mid-IR spectroscopic observations with BASS are also overlaid on the plot.

and polysulfone to superimpose absorption features for reference.

2.4. Historical UKIRT and ESO IR Photometry

We present historical IR *JHKL*'*M* photometry of NaSt1 taken from the 3.8 m United Kingdom Infrared Telescope (UKIRT) and the European Southern Observatory (ESO) 1 m photometric telescope between 1983 July and 1989 May (MJD 45528–47671). The UKIRT

and ESO photometry taken on 1983 July 13 (MJD 45838) and 1983 May 18 (MJD 45528), respectively, were previously published by Williams et al. (1987). Subsequent photometry is presented in this work for the first time. Since these observations were taken as a continuation of the photometry published by Williams et al. (1987), the observations follow the same procedures described in their paper.

Table 2. NaSt1 Historical IR Magnitudes

MJD	<i>J</i>	<i>H</i>	<i>K</i>	<i>L'</i>	<i>M</i>	Source
45528	9.54	8.51	6.50	4.12		UKIRT*
45838	9.52	8.46	6.39	3.99	3.30	ESO*
46237	9.19	8.27	6.25	3.90	3.46	UKIRT
46302	9.05	7.95	5.94	3.78	3.16	UKIRT
46715	9.49	8.18	6.19	3.91	3.18	UKIRT
46960	9.10	7.82	5.88	3.71	3.04	ESO
47258	8.99	7.85	5.87	3.66	2.98	ESO
47259	8.99	7.82	5.87	3.66	3.02	ESO
47261	9.04	7.89	5.87	3.68	2.96	ESO
47304	9.18	7.97	6.02	3.76	3.12	ESO
47670	9.40	8.25	6.25	3.89	3.19	ESO
47671	9.39	8.25	6.25	3.90	3.23	ESO

NOTE—IR photometry of NaSt1 from UKIRT and the ESO 1 m photometric telescope. Uncertainties are assumed to be 0.1 mag for *JHKL'*-band photometry and 0.15 mag for *M*-band photometry.

*Previously published by (Williams et al. 1987).

UKIRT *JHKL'* photometry was obtained using a 12.4'' diameter aperture, and *M* photometry was obtained with a 5'' diameter aperture. ESO photometry was measured through a 15'' diameter aperture except for the observation taken on 1987 June 14 (MJD 46960), where a 22'' diameter aperture was used. The photometry is shown in Table 2 and provided in Vega magnitudes.

2.5. Archival Optical Photometry: ZTF and ASAS-SN

We utilize the *g*-band and *r*-band photometry of NaSt1 from the Zwicky Transient Facility (ZTF; Bellm et al. 2019; Masci et al. 2019) Public Data Release 4⁴. ZTF observations of NaSt1 were taken between 2018 Apr. and 2020 June with a ~ 1 d cadence when visible. Only the photometry with clean extractions (i.e., “catflags = 0”) from ZTF DR4 were used for the analysis. High-cadence *r*-band observations of the field covering NaSt1 were taken on MJD 58347 and MJD 58348, where each night consisted of ~ 100 images. Instead of using all of the high-cadence photometry on MJD 58347 and MJD 58348 in the NaSt1 analysis, the average *r*-band magnitude of each night was used and the MJD provided is the time-averaged MJD of all observations in each respective night. Since ZTF photometry from the DR4 catalog was provided in units of AB magni-

⁴ <https://www.ztf.caltech.edu/page/dr4>

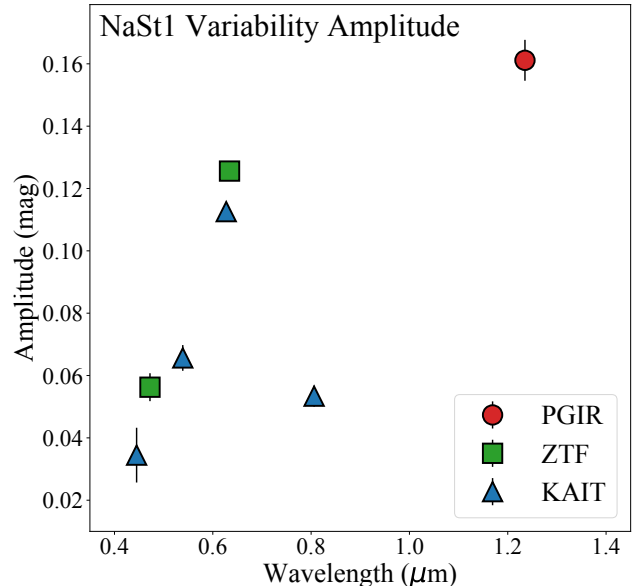


Figure 2. NaSt1 variability amplitudes from the fixed-period fits to the PGIR, ZTF, and KAIT light curves.

tude, we converted the photometry to Vega units by applying the conversions $m_{g,AB} - m_{g,Vega} = -0.08$ and $m_{r,AB} - m_{r,Vega} = 0.16$.

Lastly, we utilize the *V*-band photometry of NaSt1 from the All-Sky Automated Survey for Supernovae (ASAS-SN; Shappee et al. 2014; Kochanek et al. 2017). Photometry of NaSt1 was obtained from the ASAS-SN Variable Star Database⁵ (Jayasinghe et al. 2020), where it was identified as a variable with the reference ID ASASSN-V J185217.55+005944.3. ASAS-SN photometry of NaSt1 spans from 2015 Feb. to 2018 Nov. with an observing cadence of ~ 1 week when visible.

3. RESULTS AND ANALYSIS

3.1. Light Curve and Periodicity

The near-IR and optical light curves of NaSt1 taken between 2014 July and 2020 Oct. are shown in Figure 1 and present clear evidence of smooth variability on a roughly year-long timescale. Sinusoidal functions were fit to the PGIR, ZTF, ASAS-SN, and KAIT photometry using a least-squares fitting routine from the *SciPy* library in *Python* v.3.8.5. The free parameters were the period, variability amplitude, magnitude offset, and phase. The sinusoidal fits to each light curve reveal variability consistent with a period of ~ 300 d. A combined sinusoidal fit was also performed to all light curves simultaneously, which provided a well-constrained period of $P_{\text{Comb}} = 305.2 \pm 1.0$ d. All other light curves were

⁵ <https://asas-sn.osu.edu/variables>

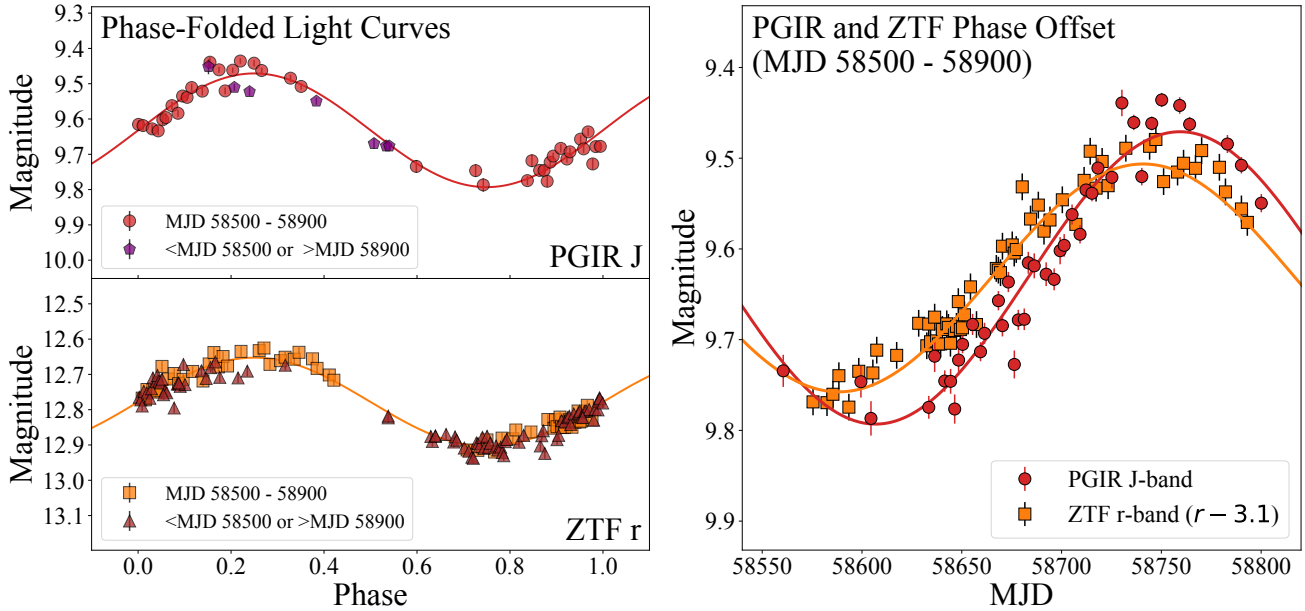


Figure 3. (*Left:*) Phase-folded PGIR J -band and ZTF r -band photometry overlaid with fixed-period sinusoidal light-curve fits. Observations obtained in the range MJD 58500–58900 are shown as red circles and orange squares for PGIR and ZTF, respectively. Observations obtained before MJD 58500 or after MJD 58900 are shown as purple pentagons or brown triangles for PGIR and ZTF, respectively. (*Right:*) Zoom-in of the PGIR J -band and ZTF r -band photometry between MJD 58500 and MJD 58900 overlaid with the fixed-period light-curve fits.

then re-fitted with a fixed period of $P = 305.2$ d. Note that the *Clear* light curve was not utilized in these fits owing to the large wavelength bandwidth of this filter. The results from the individual-filter and fixed-period sinusoidal fits are shown in Table 3. The following analysis utilizes the results from the fixed-period sinusoidal fits.

Interestingly, the sinusoidal variability amplitudes are different at the different wavelengths, which is shown in Fig. 2. Although there appears to be a general trend of increasing amplitude with wavelength between B - and J -band, the relatively low amplitude of the KAIT I -band light curve is inconsistent with this trend. The KAIT I -band amplitude is comparable to the ZTF g -band amplitude, which is a factor of ~ 2 smaller than the KAIT R - and ZTF r -band amplitudes (Tab. 3).

The amplitude fit from the ASAS-SN V -band photometry is discrepant with the KAIT V -band amplitude despite the similar wavelength coverage of the instrument filters (Tab. 3). Owing to the much larger $8''$ pixels of ASAS-SN compared to the $0''.8$ KAIT pixels and the two-pixel ($16''$) radius aperture used for ASAS-SN photometry (Kochanek et al. 2017), the lower ASAS-SN amplitude is likely due to confusion with a nearby source of comparable V -band brightness as NaSt1. Photometry from the Pan-STARRS Data Release 1 catalog (Chambers et al. 2016) supports this explanation and shows that there is a source located $\sim 16''$ from NaSt1 with

a PS1 g -band brightness 57% that of NaSt1. Synthetic Johnson V -band photometry derived from optical spectroscopy of NaSt1 presented by Crowther & Smith (1999), where $V = 14.47$ mag, also shows closer agreement with the 14.41 mag offset derived from the KAIT V -band light-curve fit (Table 3). The 0.066 ± 0.004 mag amplitude derived from the KAIT V -band photometry therefore more accurately traces the NaSt1 variability than the lower-amplitude ASAS-SN photometry.

The phase-folded PGIR J -band and ZTF r -band light curves, which show the highest variability amplitude, are shown in Figure 3 (*Left*) and demonstrate the close agreement to sinusoidal variability. The phase-folded ZTF r -band light curve in Figure 3 (*Left*) also shows the consistent sinusoidal variability over multiple cycles. The same appears true for the PGIR J -band light curve; however, there are only a few measurements outside of the cycle covered by observations between MJD 58550 and MJD 58800.

The ZTF r -band and PGIR J -band light curves from NaSt1 between MJD 58550 and MJD 58800 and the fixed-period sinusoidal fits indicate a significant ($> 5\sigma$) phase offset of ~ 18 d (Fig. 3, *Right*). There is evidence of a similar phase offset between the ZTF r -band and g -band light-curve fits, where the fixed-period g offset agrees with the fixed-period PGIR J offset within the uncertainties (Table 3). Phase offsets in NaSt1’s variability may be linked to the wavelength of the emis-

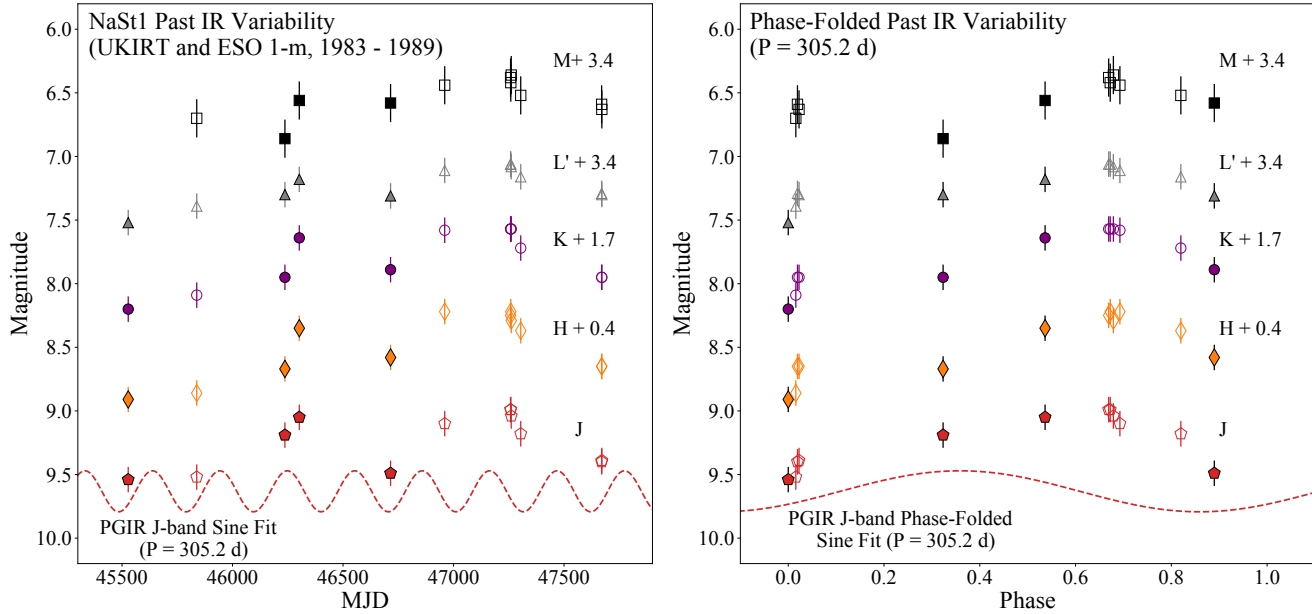


Figure 4. (Left:) $JHKLM$ -band photometry of NaSt1 observed from UKIRT (filled markers) and the ESO 1 m telescope (open markers) in the years 1983–1989 (MJD 45528–47671). The extrapolated variability from the PGIR J -band fixed-period light-curve fit is overlaid on the plot (red dashed line). (Right:) Phase-folded IR light curves assuming a 305.2 d period overlaid with the phase-folded fixed-period PGIR light curve model. Uncertainties in both plots are assumed to be 0.1 mag for $JHKLM$ photometry and 0.15 mag for M photometry.

sion, where variations in the near-IR lag behind the optical emission. Interestingly, despite the similar overlap in wavelengths between the ZTF r -band and KAIT R -band filters, there is also evidence of a ~ 20 d phase offset between the fixed-period fits to each light curve. However, uncertainties on the phase offsets are greater for the KAIT light-curve fits than the ZTF fits.

3.2. Historical IR Variability

UKIRT and ESO 1 m IR observations of NaSt1 in the years 1983–1989 exhibit IR variability exceeding the periodic behavior observed by PGIR. Figure 4 (Left) shows that several of the past J -band observations are consistent with the range of values predicted from the fixed-period PGIR J sinusoidal fit; however, observations taken in 1985 (MJD 46237, 46302), 1987 (MJD 46960), and 1988 (MJD 47258–47304) captured J emission from NaSt1 exceeding the PGIR light curve at peak brightness by 0.3–0.5 mag. Simultaneous UKIRT and ESO 1 m photometry in $HKL'M$ confirm the photometric excursions.

Figure 4 (Right) shows the phase-folded light curve of the UKIRT and ESO 1 m observations using the date of the first observation (MJD 45528) as $\varphi = 0$ and assuming a 305.2 d period. The phase-folded light curves indicate possible periodic variability on a ~ 300 d timescale; however, the peak emission appears offset by $\Delta\varphi \sim 0.4$ compared to the phase-folded PGIR light curve. The

phase-folded J light curve is also brighter by ~ 0.5 mag in comparison to the PGIR light curve. The historical IR light curves therefore indicate that NaSt1 exhibited variability on timescales of decades in addition to the periodic ~ 300 d sinusoidal variability.

3.3. Mid-IR Variability

Mid-IR spectroscopy of NaSt1 with BASS taken in 2017–2019 reveals variability at 3–13 μm (Fig. 5), where the mid-IR flux from NaSt1 is likely dominated by thermal emission from circumstellar dust (Crowther & Smith 1999; Rajagopal et al. 2007). The IR-dominated spectral energy distribution (SED) in Figure 5 also demonstrates that NaSt1 is enshrouded by circumstellar dust in addition to being obscured by interstellar material.

Semicontemporaneous ZTF gr and PGIR J photometry taken within 20 d ($\Delta\varphi \approx 0.07$) of the BASS spectroscopy in 2019 Apr. (MJD 58579) and within 5 days ($\Delta\varphi \approx 0.02$) of BASS spectroscopy in 2019 Aug. (MJD 58719) samples near the NaSt1 minimum and peak emission, respectively (Fig. 1). The NaSt1 SED at these two epochs shows that the trend in the mid-IR variability is consistent with the optical/near-IR variability (Fig. 5). The g , r , and J photometry increased by $10 \pm 4\%$, $28 \pm 2\%$, and $24 \pm 2\%$ (respectively) between the 2019 Apr. and 2019 Aug. observations shown in Figure 5. The 3–13 μm emission increased by ~ 10 –30% between

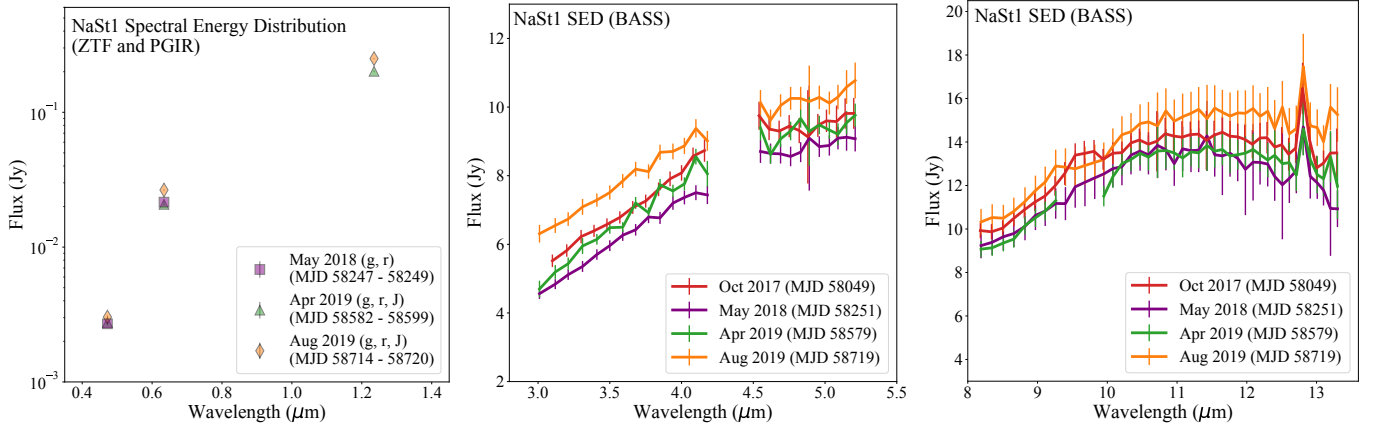


Figure 5. NaSt1 spectral energy distribution variability demonstrated by ZTF *gr*-band and PGIR *J*-band photometry and BASS mid-IR 3–13 μm low-resolution spectroscopy. The ZTF and PGIR photometry shown was obtained within at most 20 d ($\Delta\varphi \approx 0.07$) from the BASS observations. Note that the ZTF and PGIR photometry is plotted on a semilogarithmic scale, whereas the BASS spectra are shown on a linear scale.

2019 Apr. and 2019 Aug., where the largest variations ($> 20\%$) were observed at shorter mid-IR wavelengths ($\lambda \approx 3 \mu\text{m}$). Variability from the circumstellar dust emission in the mid-IR is therefore likely linked to the optical/near-IR variability.

3.4. Color Variability

In order to investigate the color variability of NaSt1, KAIT and ZTF/PGIR color curves were produced with simultaneous or nearly contemporaneous observations. Figure 6 (*Left*) presents KAIT $V - I$, $V - R$, and $R - I$ color curves, which are derived directly from the simultaneous multiband KAIT observations. Since PGIR and ZTF observations were not performed simultaneously, the PGIR/ZTF $g - J$, $g - r$, and $r - J$ light curves in Figure 6 (*Right*) were produced by utilizing observations taken within < 3 d ($\Delta\varphi < 0.01$).

KAIT color curves in Figure 6 (*Left*) each show different variability trends. The $V - R$ curve shows reddening consistent with increasing R -band brightness; however, the $R - I$ curve indicates the opposite trend with bluer colors with increasing R -band brightness. The $V - I$ curve reveals no significant variability. This is likely due to the lower amplitude of the I -band variability relative to that of the shorter wavelength R -band filter (Fig. 2). The ZTF and PGIR $g - J$, $g - r$, and $r - J$ color curves all indicate a trend in reddening correlated with increasing r -band brightness. The discrepancies in the color evolution reflect the inconsistency of the variability amplitude from NaSt1 as a function of wavelength. The observed phase offsets between different filters (Fig. 3, *Right*) likely influence the color evolution as well.

3.5. Emission-Line Contributions

Optical and near-IR spectroscopy of NaSt1 by Crowther & Smith (1999) revealed prominent narrow nebular emission lines such as He I $\lambda 6678$, $H\alpha$, and $[\text{N II}] \lambda 5755$, which may contribute to the photometric measurements. In order to determine whether the emission lines are influencing the variability, the NaSt1 emission-line list from Crowther & Smith (1999) was used to quantify the relative observed flux density contribution to the fixed-period model-fit photometry (i.e., “Mag. Offset” in Table 3). A 10% absolute flux calibration uncertainty was assumed for both the emission-line measurements from Crowther & Smith (1999) and the PGIR, KAIT, ZTF, and ASAS-SN photometry.

Table 3 shows $F_{\text{line}}/F_{\text{phot}}$, the ratio of the flux density from NaSt1’s observed emission lines over the filter bandwidths relative to the observed photometry. The nebular emission lines from NaSt1 do indeed appear to contribute more than $\sim 10\%$ to the $BgVrR$ photometry, where the strongest optical/near-IR emission lines in NaSt1 are associated with He I, He II, and $[\text{N II}]$. However, the emission line contribution is much lower in I and J . Since the amplitudes in the $BgVrR$ light curves are in the range ~ 0.04 – 0.13 mag, or $\sim \pm 4$ – 11% of the “Mag. Offset,” it is possible that the photometric variability may be due to changes in the observed strength of the emission lines in these filters. The lack of any significant line contribution for the PGIR J -band observations, the large J variability amplitude, and its observed phase offset may indicate that the near-IR emission originates from a different component than the optical emission in NaSt1.

4. DISCUSSION

4.1. Possible Origins of Variability

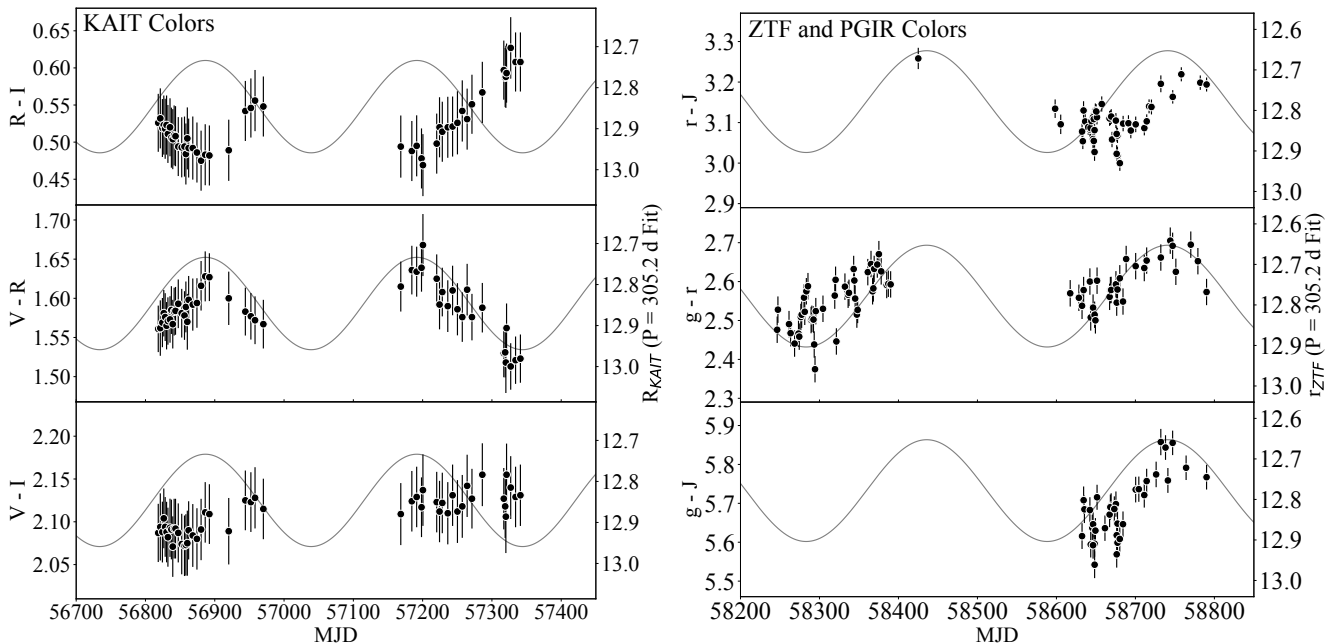


Figure 6. (Left) KAIT $V - I$, $V - R$, and $R - I$ colors between MJD 56800 and MJD 57350 overlaid with the KAIT R -band fixed-period sinusoidal model light curve. (Right) ZTF and PGIR $g - J$, $g - r$, and $r - J$ colors between MJD 58200 and MJD 58800 overlaid with the ZTF r -band fixed-period sinusoidal model light curve.

Although individual hot massive stars are known to exhibit variability, their photometric variations do not typically appear as regular or sinusoidal as we observe from NaSt1 (e.g., Soraisam et al. 2020). An exception to this is the rare class of magnetic O-type stars with the peculiar “Of?p” classification that exhibit periodic variability that is believed to be associated with rotational modulation (Howarth et al. 2007; Grunhut et al. 2017). However, Of?p stars are characterized by the presence of strong N III $\lambda 4634$ – 4641 and C III $\lambda 4650$ emission lines (Walborn 1973), which are weak or absent in NaSt1 (Crowther & Smith 1999).

We therefore claim that the variability is associated with the orbital period of a binary system in NaSt1. In this section, we discuss the possible origins of NaSt1’s photometric variability and the relation to its orbital period.

First, we can obtain a clearer understanding of the binary system in NaSt1 from the ~ 300 d orbital period. Assuming a combined stellar mass in the range ~ 20 – $100 M_{\odot}$ for the binary and a circular orbit, NaSt1’s ~ 300 d orbital period corresponds to an orbital separation of ~ 2 – 4 au. We note that a circular orbit is expected for a system that recently underwent RLOF. The orientation of the binary system can be inferred from its extended N-rich nebula, which exhibits a nearly edge-on geometry with an inclination angle of $i = 78^{\circ} \pm 3^{\circ}$ (Mauerhan et al. 2015). Figure 7 (Top) shows the resolved *HST* imaging by Mauerhan et al.

(2015) of NaSt1’s N-rich nebula and our schematic illustration of the embedded central binary. Given this information on the orbital properties of the binary, we consider three different possibilities that may contribute to the observed variability (Fig. 7, Bottom): disk eclipses, colliding-wind dust formation, and ellipsoidal variability.

Disk Eclipses. Given the large orbital separation ranging over several au, it is highly unlikely that the smooth, sinusoidal variability is due to eclipses from the stars themselves, which would instead appear as narrow eclipses. However, we suggest that the variability may be caused by eclipses of a circumbinary disk from an optically and geometrically thick circumstellar disk in NaSt1 that formed as a result of the RLOF mass-transfer process. Several prominent emission lines in NaSt1 (e.g., [N II] $\lambda 5755$; Crowther & Smith 1999) show double-peaked profiles that indeed indicate the presence of a disk.

This scenario is similar to the massive eclipsing binary RY Scuti, which is currently undergoing RLOF with a mass gainer that appears to be enshrouded by an optically and geometrically thick accretion disk (Grundstrom et al. 2007; Djurašević et al. 2008; Smith et al. 2011b). RY Scuti also exhibits smooth, periodic variability; however, its 11 d orbital period is much shorter than that of NaSt1, and its variability is not as consistent with a sine wave (Djurašević et al. 2008).

Table 3. NaSt1 Light-Curve Properties

Telescope (Filter)	Period (d)	Amplitude (mag)	Mag. Offset	MJD ($\varphi = 0$)	$\Delta\varphi$ (d)	$F_{\text{line}}/F_{\text{phot}}$	Brightest Lines
PGIR (<i>J</i>) 12350 Å (1624 Å)	296.4 ± 4.7	0.155 ± 0.007 [0.161 \pm 0.007]	9.622 ± 0.007 [9.632 \pm 0.006]	58687.1 ± 2.8 [58683.1 \pm 2.1]	0.0 ± 2.8 [0.0 \pm 2.1]	< 0.01	He I λ 12785 He I λ 12526 Pa β
KAIT (<i>I</i>) 8061 Å (1471 Å)	291.0 ± 5.2	0.052 ± 0.003 [0.053 \pm 0.003]	12.295 ± 0.003 [12.301 \pm 0.002]	56822.9 ± 3.7 [56814.6 \pm 2.5]	-117.9 ± 31.4 [-37.5 \pm 6.1]	0.05 ± 0.01	He II λ 8237 O I λ 8446 [N I] λ 8680
ZTF (<i>r</i>) 6340 Å (1515 Å)	307.6 ± 1.3	0.126 ± 0.003 [0.126 \pm 0.003]	12.778 ± 0.002 [12.778 \pm 0.002]	58665.9 ± 1.4 [58664.6 \pm 1.2]	-21.1 ± 3.1 [-18.5 \pm 2.1]	0.23 ± 0.03	He I λ 6678 He I λ 5876 H α
KAIT (<i>R</i>) 6273 Å (1202 Å)	299.4 ± 2.6	0.111 ± 0.003 [0.113 \pm 0.003]	12.841 ± 0.003 [12.846 \pm 0.002]	56813.6 ± 1.9 [56810.2 \pm 1.2]	-77.0 ± 15.9 [-41.9 \pm 6.1]	0.29 ± 0.04	He I λ 6678 He I λ 5876 H α
ASAS-SN* (<i>V</i>) 5466 Å (890 Å)	303.8 ± 3.2	0.033 ± 0.003 [0.033 \pm 0.003]	14.025 ± 0.002 [14.025 \pm 0.002]	57131.8 ± 7.4 [57129.0 \pm 4.4]	-36.5 ± 17.6 [-28.3 \pm 5.2]	0.24 ± 0.03	He I λ 5876 [N II] λ 5755 He II λ 5412
KAIT (<i>V</i>) 5389 Å (909 Å)	295.8 ± 5.2	0.066 ± 0.004 [0.066 \pm 0.004]	14.409 ± 0.003 [14.412 \pm 0.003]	56805.3 ± 4.4 [56799.1 \pm 3.0]	-107.1 ± 31.5 [-53.0 \pm 6.1]	0.12 ± 0.02	[N II] λ 5755 He I λ 5016 He II λ 5412
ZTF (<i>g</i>) 4722 Å (1282 Å)	303.1 ± 4.4	0.056 ± 0.005 [0.056 \pm 0.004]	15.346 ± 0.004 [15.345 \pm 0.003]	58679.1 ± 4.6 [58680.7 \pm 3.6]	-8.0 ± 5.4 [-2.4 \pm 2.1]	0.15 ± 0.02	He II λ 4686 He I λ 5016 H β
KAIT (<i>B</i>) 4445 Å (907 Å)	274.8 ± 13.6	0.036 ± 0.008 [0.034 \pm 0.009]	16.200 ± 0.006 [16.207 \pm 0.006]	56831.2 ± 10.3 [56814.3 \pm 8.9]	-207.1 ± 82.4 [-37.8 \pm 6.1]	0.24 ± 0.03	He II λ 4686 H β [Fe III] λ 4658

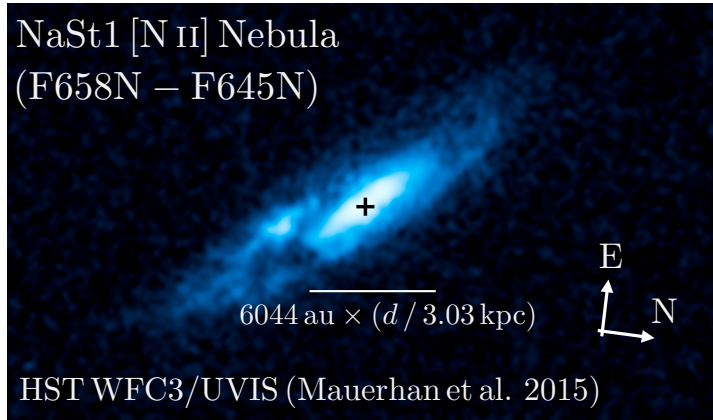
NOTE—NaSt1 photometry and light-curve properties from individual-filter and fixed-period (in brackets) fits showing the telescope/instrument with the filter effective wavelength and bandwidth, the derived period, the amplitude of the sinusoidal variability, the magnitude offset at mid-line of the sine function, the MJD where the phase $\phi = 0$, and the phase offset ($\Delta\varphi$) from the PGIR value. The phase fitting for the ZTF and PGIR models assumed an initial $\phi = 0$ estimate of MJD 58700, while the KAIT and ASAS-SN models assumed initial $\phi = 0$ estimates of MJD 57100 and MJD 56800, respectively. The fixed-period fits use $P_{\text{comb}} = 305.2$ d, which is derived from a combined sinusoidal fit to all light curves simultaneously. The relative flux contributions from the cataloged nebular emission lines from NaSt1 (Crowther & Smith 1999) to the photometric measurements in the different filters wavebands (based on the fixed-period fit) is shown under $F_{\text{line}}/F_{\text{phot}}$. The brightest three lines in each filter band is also listed in descending order of line strength.

*ASAS-SN photometry of NaSt1 is likely confused with a nearby ($\sim 16''$) optical point source.

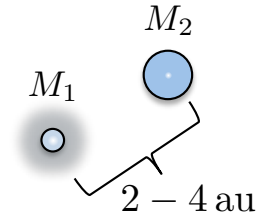
Given the significant contribution from the strong nebular emission lines to the observed photometry in NaSt1 (Table 3), it is possible that the photometric variability is linked to the obscuration of line-emitting regions from a circumbinary disk by the circumstellar disk. Optical variability in this scenario could arise from a circumstellar disk obscuring a varying fraction of the emitting surface area from a circumbinary disk, which also requires the density distribution of the circumbinary disk to not be circularly symmetric. This may be expected if circumbinary material is associated with NaSt1’s asymmetric [N II] nebula (Fig. 7). The

observed IR variability may arise from disk eclipses of the observed circumstellar/circumbinary dust component around NaSt1 with an extent of $\lesssim 150$ au (Rajagopal et al. 2007).⁶ A similar alternative scenario is that a circumstellar disk may block a significant fraction of the ionizing and dust-heating radiation field from the stripped-envelope star. If the surrounding nebulae of dust and ionized gas are asymmetric, this scenario could

⁶ This has been updated with the recent $d = 3.03$ kpc distance estimate to NaSt1 (Rate & Crowther 2020), and we note that Rajagopal et al. (2007) had adopted a distance of 2 kpc.



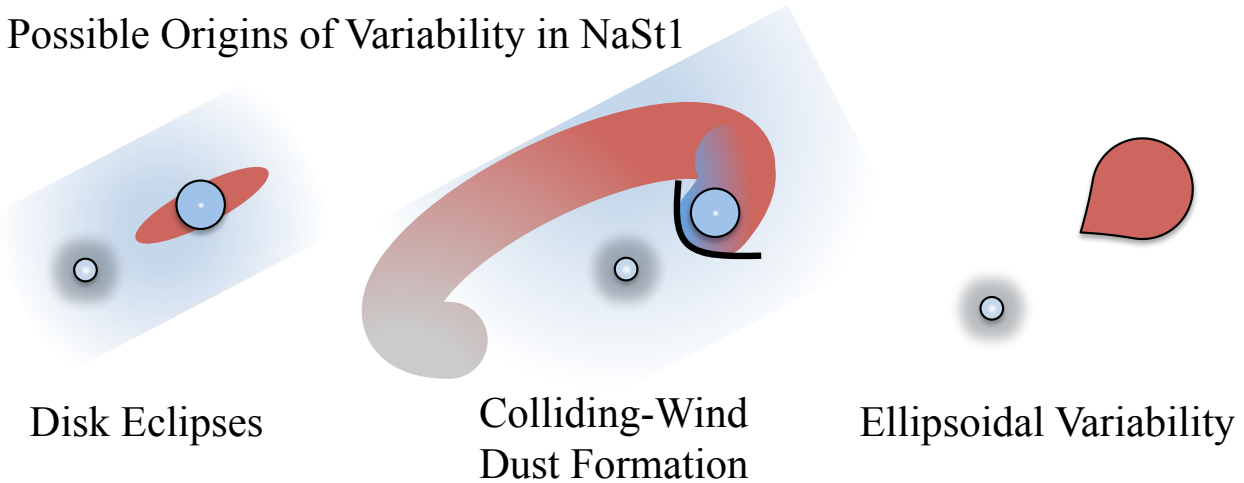
NaSt1 Central Binary



$$P \approx 300 \text{ d}$$

$$M_1 + M_2 \approx 20 - 100 M_{\odot} \text{ (Assumed)}$$

Possible Origins of Variability in NaSt1



Disk Eclipses

Colliding-Wind
Dust Formation

Ellipsoidal Variability

Figure 7. (Top Left:) HST/WFC3/UVIS image of the extended [N II] nebula around NaSt1 from Mauerhan et al. (2015) and (Top Right:) schematic illustration of the central binary of NaSt1 overlaid with the derived orbital properties, where M_1 is the stripped-envelope star and M_2 is the mass gainer. (Bottom:) Schematic illustrations of the possible origins of variability in NaSt1: disk eclipses, colliding-wind dust formation, and ellipsoidal variability. Note that the illustrations in this figure are not drawn to scale.

also lead to optical/IR variability throughout the orbit of the central binary.

Colliding-wind Dust Formation. Mid-IR and X-ray observations of NaSt1 indicate the presence of ongoing or recent dust formation that may be due to colliding winds (Rajagopal et al. 2007; Mauerhan et al. 2015). Dust formation via colliding winds is common in late-type carbon-rich WR (WC) binaries (Williams et al. 1987) and is also believed to occur in η Car (Smith 2010). In this process, the strong wind from the WR star collides with the weaker wind from an OB-star companion which creates a dense shock front that cools and forms dust in the wake of the OB star (Usov 1991; Tuthill et al. 2008). An inclined dust-forming WR binary can exhibit smooth IR variability owing to viewing perspective variations toward the dust-forming region throughout the system’s orbit (Monnier et al. 1999; Hendrix et al. 2016). The line-of-sight optical depth to the dust-forming regions can vary with viewing angle due to obscuration

from optically thick regions of the colliding-wind shock cone. These effects are evident in the colliding-wind dust-forming WR system WR 98a (WC8-9vd; Williams et al. 1995), which exhibits a “rotating” dusty pinwheel nebula and near-sinusoidal IR variability that are both consistent with a ~ 565 d period (Monnier et al. 1999).

NaSt1 does not exhibit an obvious dusty pinwheel nebula; however, it may be difficult to resolve owing to its shorter orbital period and high inclination. We therefore suggest that the near-IR and mid-IR variability from NaSt1 may be due to a mechanism similar to that seen in WR 98a. In this scenario, the optical variability observed from NaSt1 could be linked to obscuration of a circumbinary nebula by optically thick regions of the colliding-wind shock cone and/or newly formed dust. We note that it is unlikely that the observed variability of NaSt1 arises from variable or episodic dust formation since we would expect anticorrelated IR and optical light

curves where newly forming IR-luminous dust obscures the optical emission.

Ellipsoidal Variability. Given the mass-transfer interaction in NaSt1, the stars and/or a circumstellar disk may be tidally distorted and exhibit ellipsoidal variability as the system reveals different cross-sections throughout its nearly edge-on orbit (e.g., [Morris & Naftilan 1993](#)). Such variations may naturally reproduce some of the wavelength-dependent amplitudes of the light curve owing to temperature gradients along the surface of the elongated star or disk.

It is important to note that if the NaSt1 light curve was modulated by ellipsoidal variability, its orbital period would be twice that of the period derived from the sinusoidal model, since two consecutive brightness peaks would correspond to the two phases of quadrature in a full orbit. Tidally elongated stars in such a wide orbital configuration would therefore have to exhibit large radii. Assuming a $2 \times 300 = 600$ d orbital period, a combined stellar mass range of 20–100 M_{\odot} , and a binary mass ratio of 0.25–4.0, the radius of the tidally distorted star would have to approach its Roche-lobe radius of 220–700 R_{\odot} ([Eggleton 1983](#)). The tidally distorted star would therefore have to possess a radius consistent with that of a supergiant.

We favor the interpretation that NaSt1’s periodic variability is linked to variable line-of-sight optical depth effects from colliding-wind dust formation. However, we cannot conclusively rule out a possible contribution from disk eclipses. In [Sec. 4.3](#), we will argue that NaSt1 is not currently undergoing RLOF mass transfer and therefore claim that ellipsoidal variability from a tidally distorted supergiant is unlikely. It is also important to note that almost all known massive dust-forming colliding-wind binaries exhibit a C-rich chemistry and host a WC star ([Crowther 2007](#)), where the exception is η Car and its N-rich circumstellar environment ([Smith et al. 2011b](#)). Future work on determining the composition of circumstellar dust around NaSt1 will be important for distinguishing the chemistry of its WR star.

There are still unresolved issues on how to account for the apparent phase delay between different filters ([Fig. 3, Right](#); [Table 3](#)) as well as the long-term variability on timescales of \sim decades ([Fig. 4](#)). Given the complexity of NaSt1, further observations and theoretical modeling are needed to resolve these issues and test our hypotheses. For example, three-dimensional radiative transfer models would be valuable for exploring how variations in line-of-sight optical depths from colliding-wind dust formation affect both optical and IR light curves. Continued multiwavelength photometric as well

as spectroscopic monitoring of NaSt1 will also be important for resolving the origin(s) of its variability.

4.2. On the Nature of NaSt1: An Ofpe/WN9 Eruption?

The ~ 2 –4 au orbital separation estimate of the binary in NaSt1 ([Sec. 4.1](#)) allows us to estimate the Roche-lobe radius that the mass-donor star must have approached in order to trigger mass transfer. Assuming a binary mass ratio of 0.25–4.0, the Roche-lobe radius is in the range 140–440 R_{\odot} . Although such a large stellar radius suggests an RSG mass donor, the H-rich chemistry of an RSG’s envelope does not appear to be consistent with the highly CNO-processed material in NaSt1’s nebula ejected from the mass-transfer process ([Crowther & Smith 1999](#); [Mauerhan et al. 2015](#)). [Crowther & Smith \(1999\)](#) notably suggest that the composition of the nebula is consistent with that of a nitrogen-rich WR (WN) star; however, they clearly demonstrate that NaSt1 does not exhibit any broad features consistent with a WN star.

Interestingly, [Smith et al. \(2020\)](#) presented observations of an Ofpe/WN9 star, which are stars that show properties intermediate between those of Of and WN stars ([Walborn 1977](#); [Bohannon & Walborn 1989](#)), and confirmed that they can undergo an LBV-like eruption. During this eruptive phase, the radius of the Ofpe/WN9 star can expand to double the size of its quiescent radius ([Smith et al. 2020](#)). Ofpe/WN9 stars in the Galactic center exhibit radii of $R_{2/3} \approx 35$ –80 R_{\odot} , which corresponds to the radius where $\tau_{\text{Rosseland}} = 2/3$ ([Martins et al. 2007](#)). We therefore suggest that mass transfer in NaSt1 may have been triggered during an eruptive phase from an Ofpe/WN9 star that is now obscured or outshined by dense circumbinary or circumstellar material.

Earlier, [van der Hucht et al. \(1989\)](#) had proposed that NaSt1 may host an Ofpe/WN9 star; however, [Crowther & Smith \(1999\)](#) argued against this based on dissimilarities of its optical spectrum compared to the WN10 star HDE 269582 (previously classified as Ofpe/WN9; [Crowther & Smith 1997](#)). [Crowther & Smith \(1999\)](#) instead suggested that NaSt1 hosts an early-type WN star based on the high temperatures required for the ionization source of its nebula. Our hypothesis on the nature of NaSt1 is still consistent with the interpretation by [Crowther & Smith \(1999\)](#): after its eruption, the WR star may no longer resemble an Ofpe/WN9 star and could have transitioned to a hotter, earlier-type WN phase (e.g., WN7) like the Ofpe/WN9 star MCA-1B studied by [Smith et al. \(2020\)](#). It is also possible that envelope stripping from the WR star in NaSt1 has led

to a more advanced chemical composition than the WN phase such as the WC phase. The deficiency of carbon in the circumstellar environment around NaSt1 would require a very recent transition to a WC star. In the following section, we indeed argue that mass transfer has recently ceased in NaSt1.

4.3. No More Mass Transfer in NaSt1

It is important to address whether the binary in NaSt1 is still interacting and undergoing RLOF. We can estimate the current radius of the WR star and compare it to the Roche-lobe radius ($R_L \approx 140\text{--}440 R_\odot$) derived above. First, we obtain an estimate of the luminosity of the system from its apparent $V = 14.4$ mag. By adopting the interstellar extinction correction toward NaSt1 by Crowther & Smith (1999) of $A_V = 6.5$ mag and using the *Gaia*-derived distance of $d = 3.03$ kpc (Rate & Crowther 2020), the absolute magnitude of NaSt1 is $M_V = -4.5$. Adopting the 30,000 K lower limit of the temperature derived for the ionizing source in NaSt1 by Crowther & Smith (1999) from optical spectroscopy, the appropriate bolometric correction is $BC_V = -3$ mag and the luminosity of the source is $L \approx 7.9 \times 10^4 L_\odot$. The radius of such a 30,000 K star is therefore $R_* \approx 10 R_\odot$, which is more than an order of magnitude from filling the Roche-lobe radius. We note that although temperatures higher than 30,000 K will require larger bolometric corrections and thus lead to higher luminosities, the resulting radii will be smaller than that of a 30,000 K star. For example, a star with a temperature of 200,000 K, which is the upper limit of the ionizing source temperature derived by Crowther & Smith (1999), would imply a luminosity of $L \approx 3.1 \times 10^6 L_\odot$ and a stellar radius of $R_* \approx 1.5 R_\odot$ given the appropriate bolometric correction of $BC_V = -7$ mag. Based on these constraints, we claim that mass transfer has ceased in NaSt1.

Assuming that the extended [N II] nebula around NaSt1 formed when the system was undergoing mass transfer (Mauerhan et al. 2015), we can provide an upper limit on how long ago mass transfer ceased. The diameter of the [N II] nebula is $6.8''$, or 21,000 au at $d = 3.03$ kpc. Assuming an expansion velocity of 15 km s^{-1} for the nebula (Crowther & Smith 1999), mass transfer must have ceased $\lesssim 3400$ yr ago in NaSt1.

5. CONCLUSIONS

We presented the discovery of a ~ 300 d period from the interacting massive binary NaSt1 with optical and near-IR light curves obtained between 2014 July and 2020 Oct. (Fig. 1). With a combined fit utilizing all light curves simultaneously, we derive a well-constrained

sinusoidal period of $P_{\text{Comb}} = 305.2 \pm 1.0$ d. The sinusoidal variability of NaSt1 exhibited different amplitudes at various wavelengths as well as a significant phase shift between the sine models fit to the r -band and J -band light curves (Table 3, Fig. 3). Based on previously cataloged optical emission lines from the nebula surrounding NaSt1 (Crowther & Smith 1999), we determine that nebular emission lines contribute more than $\sim 10\%$ to the $BgVr$ photometry (Table 3) and may therefore be linked to the differing variability amplitudes at each wavelength filter. Historical IR light curves from 1983–1989 suggest that NaSt1 exhibits variability on \sim decade timescales in addition to its periodic ~ 300 d sinusoidal variability (Fig. 4). Mid-IR spectra of NaSt1, which were taken semicontemporaneously with ZTF and PGIR observations, demonstrated that its $3\text{--}13 \mu\text{m}$ emission is also variable and appears to be correlated with the optical/near-IR variability (Fig. 5).

We claim that the ~ 300 d optical/near-IR periodic, sinusoidal variability is associated with the orbital period of a binary system in NaSt1, thus confirming its binary nature. Although the properties of the stars in this binary system are still unknown, we use the ~ 300 d orbital period to estimate an orbital separation of $\sim 2\text{--}4$ au assuming the total combined mass of the binary is $20\text{--}100 M_\odot$ (Fig. 7, Top).

Given the nearly edge-on geometry of NaSt1’s extended nebula (Mauerhan et al. 2015), we present possible origins of variability including (1) eclipses of a circumbinary disk from an optically and geometrically thick circumstellar disk around one of the stars, (2) variations in the line-of-sight optical depth to optical/near-IR emitting regions due to colliding-wind dust formation, and (3) ellipsoidal variability from a tidally elongated star (Fig. 7, Bottom). We favor the colliding-wind dust formation hypothesis; however, future work with 3D radiative transfer modeling is crucial to reproduce optical and IR light curves that incorporate the line-of-sight optical depth variability throughout the orbit of a highly inclined dust-forming colliding-wind binary. Additionally, the explanation for the observed phase offsets and long-term variability are still open questions.

Based on the CNO-enriched material in NaSt1’s nebula and the estimated range of sizes for the Roche-lobe radius of the mass donor star in NaSt1 ($\sim 140\text{--}440 R_\odot$), we suggest that mass transfer was triggered by an LBV-like eruptive phase in an Ofpe/WN9 star in NaSt1 that filled its Roche lobe as it expanded. This interpretation is bolstered with recent observations by Smith et al. (2020) that confirmed Ofpe/WN9 stars can undergo LBV-like eruptions and expand to double the size of their quiescent radius. Owing to the mass loss from

its outer envelope, it is possible that the WR star in NaSt1 no longer resembles an Ofpe/WN9 star. The WR star may have transitioned to either a hotter, earlier WN spectral subtype or a more chemically advanced WC phase. Lastly, based on the inferred orbital separation, radius estimates of the star that dominates the V-band emission, and the extent of its [N II] nebula, we conclude that the binary in NaSt1 recently ($\lesssim 3400$ yr) ceased RLOF mass transfer.

The results we presented on NaSt1 provide new insights into an important transitional evolutionary phase of massive stars. NaSt1 is notably one of the few systems known from which we can probe this binary mass-transfer process. Multiwavelength follow-up observations and continued spectroscopic and photometric monitoring will therefore be valuable for addressing the open questions that remain on the nature of NaSt1.

We thank T. Jayasinghe for discussion of the technical details of the filter properties in the ASAS-SN survey. R.M.L. acknowledges the Japan Aerospace Exploration Agency’s International Top Young Fellowship (ITYF). A.F.J.M. is grateful for financial assistance from NSERC (Canada). M.M.K. acknowledges the Heising-Simons foundation for support via a Scialog fellowship of the Research Corporation. M.M.K. and A.M.M. acknowledge the Mt. Cuba Astronomical Foundation. A.V.F. is grateful for financial assistance from the TABASGO Foundation, the Christopher R. Redlich Fund, and the U.C. Berkeley Miller Institute for Basic Research in Science (where he is a Miller Senior Fellow). M.M.K. acknowledges generous support from the David and Lucille Packard Foundation. J.S. is supported by an Australian Government Research Training Program (RTP) Scholarship.

Palomar Gattini-IR (PGIR) is generously funded by Caltech, Australian National University, the Mt. Cuba Astronomical Foundation, the Heising-Simons Foundation, and the Binational Science Foundation. PGIR is a collaborative project among Caltech, Australian National University, University of New South Wales, Columbia University, and the Weizmann Institute of Science. Based in part on observations obtained with the Samuel Oschin 48-inch Telescope at the Palomar Observatory as part of the Zwicky Transient Facility

project. ZTF is supported by the National Science Foundation (NSF) under grant AST-1440341 and a collaboration including Caltech, IPAC, the Weizmann Institute for Science, the Oskar Klein Center at Stockholm University, the University of Maryland, the University of Washington, Deutsches Elektronen-Synchrotron and Humboldt University, Los Alamos National Laboratories, the TANGO Consortium of Taiwan, the University of Wisconsin at Milwaukee, and Lawrence Berkeley National Laboratories. Operations are conducted by Caltech Optical Observatories, IPAC, and the University of Washington. We thank the Las Cumbres Observatory and its staff for its continuing support of the ASAS-SN project. LCOGT observations were performed as part of DDT award 2019B003 to E.G. ASAS-SN is supported by the Gordon and Betty Moore Foundation through grant GBMF5490 to the Ohio State University, and NSF grants AST-1515927 and AST-1908570. Development of ASAS-SN has been supported by NSF grant AST-0908816, the Mt. Cuba Astronomical Foundation, the Center for Cosmology and AstroParticle Physics at the Ohio State University, the Chinese Academy of Sciences South America Center for Astronomy (CAS-SACA), the Villum Foundation, and George Skestos. UKIRT is owned by the University of Hawaii (UH) and operated by the UH Institute for Astronomy; operations are enabled through the cooperation of the East Asian Observatory. When the data reported here were acquired, UKIRT was operated by the Joint Astronomy Centre on behalf of the Science and Technology Facilities Council of the U.K. Research at Lick Observatory is partially supported by a generous gift from Google. KAIT and its ongoing operation were made possible by donations from Sun Microsystems, Inc., the Hewlett-Packard Company, AutoScope Corporation, Lick Observatory, the NSF, the University of California, the Sylvia & Jim Katzman Foundation, and the TABASGO Foundation.

This research made use of Astropy,⁷ a community-developed core Python package for Astronomy ([Astropy Collaboration et al. 2013, 2018](http://www.astropy.org)).

Facilities: PGIR, KAIT, ZTF, ASAS-SN, AEOS (BASS), UKIRT, ESO 1-m

REFERENCES

- Astropy Collaboration, Robitaille, T. P., Tollerud, E. J., et al. 2013, *A&A*, 558, A33
 Astropy Collaboration, Price-Whelan, A. M., Sipőcz, B. M., et al. 2018, *AJ*, 156, 123

⁷ <http://www.astropy.org>

- Belczynski, K., Holz, D. E., Bulik, T., et al. 2016, *Nature*, 534, 512. doi:10.1038/nature18322
- Bellm, E. C., Kulkarni, S. R., Graham, M. J., et al. 2019, *PASP*, 131, 018002. doi:10.1088/1538-3873/aaecbe
- Bohannon, B. & Walborn, N. R. 1989, *PASP*, 101, 520. doi:10.1086/132463
- Chambers, K. C., Magnier, E. A., Metcalfe, N., et al. 2016, arXiv:1612.05560
- Crowther, P. A. & Smith, L. J. 1997, *A&A*, 320, 500
- Crowther, P. A. & Smith, L. J. 1999, *MNRAS*, 308, 82. doi:10.1046/j.1365-8711.1999.02707.x
- Crowther, P. A. 2007, *ARA&A*, 45, 177. doi:10.1146/annurev.astro.45.051806.110615
- Cutri, R. M., Skrutskie, M. F., van Dyk, S., et al. 2003, *VizieR Online Data Catalog*, II/246
- De, K., Hankins, M. J., Kasliwal, M. M., et al. 2020, *PASP*, 132, 025001. doi:10.1088/1538-3873/ab6069
- De, K., Ashley, M. C. B., Andreoni, I., et al. 2020, *ApJL*, 901, L7. doi:10.3847/2041-8213/abb3c5
- De Marco, O. & Izzard, R. G. 2017, *PASA*, 34, e001. doi:10.1017/pasa.2016.52
- Djurašević, G., Vince, I., & Atanacković, O. 2008, *AJ*, 136, 767. doi:10.1088/0004-6256/136/2/767
- Eggleton, P. P. 1983, *ApJ*, 268, 368. doi:10.1086/160960
- Filippenko, A. V., Li, W. D., Treffers, R. R., et al. 2001, *IAU Colloq. 183: Small Telescope Astronomy on Global Scales*, 246, 121
- Gaia Collaboration 2018, *VizieR Online Data Catalog*, I/345
- Ganeshalingam, M., Li, W., Filippenko, A. V., et al. 2010, *ApJS*, 190, 418. doi:10.1088/0067-0049/190/2/418
- Gehrz, R. D., Hayward, T. L., Houck, J. R., et al. 1995, *ApJ*, 439, 417. doi:10.1086/175184
- Götberg, Y., de Mink, S. E., Groh, J. H., et al. 2018, *A&A*, 615, A78. doi:10.1051/0004-6361/201732274
- Götberg, Y., de Mink, S. E., McQuinn, M., et al. 2020, *A&A*, 634, A134. doi:10.1051/0004-6361/201936669
- Groh, J. H., Meynet, G., & Ekström, S. 2013, *A&A*, 550, L7. doi:10.1051/0004-6361/201220741
- Grundstrom, E. D., Gies, D. R., Hillwig, T. C., et al. 2007, *ApJ*, 667, 505. doi:10.1086/521043
- Grunhut, J. H., Wade, G. A., Neiner, C., et al. 2017, *MNRAS*, 465, 2432. doi:10.1093/mnras/stw2743
- Hackwell, J. A., Warren, D. W., Chatelain, M. A., et al. 1990, *Proc. SPIE*, 1235, 171. doi:10.1117/12.19086
- Heger, A., Fryer, C. L., Woosley, S. E., et al. 2003, *ApJ*, 591, 288. doi:10.1086/375341
- Hendrix, T., Keppens, R., van Marle, A. J., et al. 2016, *MNRAS*, 460, 3975. doi:10.1093/mnras/stw1289
- Howarth, I. D., Walborn, N. R., Lennon, D. J., et al. 2007, *MNRAS*, 381, 433. doi:10.1111/j.1365-2966.2007.12178.x
- Jayasinghe, T., Stanek, K. Z., Kochanek, C. S., et al. 2020, *MNRAS*, 493, 4186. doi:10.1093/mnras/staa499
- Kochanek, C. S., Shappee, B. J., Stanek, K. Z., et al. 2017, *PASP*, 129, 104502. doi:10.1088/1538-3873/aa80d9
- Landolt, A. U. 1992, *AJ*, 104, 340. doi:10.1086/116242
- Lau, R. M., Eldridge, J. J., Hankins, M. J., et al. 2020, *ApJ*, 898, 74
- Li, W., Filippenko, A. V., Chornock, R., et al. 2003, *PASP*, 115, 844. doi:10.1086/376432
- Masci, F. J., Laher, R. R., Rusholme, B., et al. 2019, *PASP*, 131, 018003. doi:10.1088/1538-3873/aae8ac
- Martins, F., Genzel, R., Hillier, D. J., et al. 2007, *A&A*, 468, 233. doi:10.1051/0004-6361:20066688
- Massey, P. & Conti, P. S. 1983, *PASP*, 95, 440. doi:10.1086/131190
- Mauerhan, J., Smith, N., Van Dyk, S. D., et al. 2015, *MNRAS*, 450, 2551. doi:10.1093/mnras/stv257
- Moe, M. & Di Stefano, R. 2017, *ApJS*, 230, 15. doi:10.3847/1538-4365/aa6fb6
- Monnier, J. D., Tuthill, P. G., & Danchi, W. C. 1999, *ApJL*, 525, L97. doi:10.1086/312352
- Moore, A. M. & Kasliwal, M. M. 2019, *Nature Astronomy*, 3, 109. doi:10.1038/s41550-018-0675-x
- Morris, S. L. & Naftilan, S. A. 1993, *ApJ*, 419, 344. doi:10.1086/173488
- Nassau, J. J. & Stephenson, C. B. 1963, *Hamburger Sternw. Warner & Swasey Obs.*, C04, 0
- Rajagopal, J., Menut, J.-L., Wallace, D., et al. 2007, *ApJ*, 671, 2017. doi:10.1086/522515
- Rate, G. & Crowther, P. A. 2020, *MNRAS*, 493, 1512. doi:10.1093/mnras/stz3614
- Sana, H., de Mink, S. E., de Koter, A., et al. 2012, *Science*, 337, 444. doi:10.1126/science.1223344
- Sander, A. A. C. & Vink, J. S. 2020, *MNRAS*, 499, 873. doi:10.1093/mnras/staa2712
- Shappee, B. J., Prieto, J. L., Grupe, D., et al. 2014, *ApJ*, 788, 48. doi:10.1088/0004-637X/788/1/48
- Smith, N. & Morse, J. A. 2004, *ApJ*, 605, 854. doi:10.1086/382671
- Smith, N. 2010, *MNRAS*, 402, 145. doi:10.1111/j.1365-2966.2009.15901.x
- Smith, N., Li, W., Filippenko, A. V., et al. 2011, *MNRAS*, 412, 1522. doi:10.1111/j.1365-2966.2011.17229.x
- Smith, N., Gehrz, R. D., Campbell, R., et al. 2011, *MNRAS*, 418, 1959. doi:10.1111/j.1365-2966.2011.19614.x
- Smith, N., Li, W., Filippenko, A. V., et al. 2011, *MNRAS*, 412, 1522. doi:10.1111/j.1365-2966.2011.17229.x

- Smith, N. 2014, *ARA&A*, 52, 487.
doi:10.1146/annurev-astro-081913-040025
- Smith, N., E Andrews, J., Moe, M., et al. 2020, *MNRAS*, 492, 5897. doi:10.1093/mnras/staa061
- Soraisam, M. D., Bildsten, L., Drout, M. R., et al. 2020, *ApJ*, 893, 11. doi:10.3847/1538-4357/ab7b7b
- Stahl, B. E., Zheng, W., de Jaeger, T., et al. 2019, *MNRAS*, 490, 3882. doi:10.1093/mnras/stz2742
- Stetson, P. B. 1987, *PASP*, 99, 191. doi:10.1086/131977
- Sukhbold, T., Ertl, T., Woosley, S. E., et al. 2016, *ApJ*, 821, 38. doi:10.3847/0004-637X/821/1/38
- Tonry, J. L., Stubbs, C. W., Lykke, K. R., et al. 2012, *ApJ*, 750, 99. doi:10.1088/0004-637X/750/2/99
- Tuthill, P. G., Monnier, J. D., & Danchi, W. C. 1999, *Nature*, 398, 487
- Tuthill, P. G., Monnier, J. D., Lawrance, N., et al. 2008, *ApJ*, 675, 698. doi:10.1086/527286
- Usov, V. V. 1991, *MNRAS*, 252, 49
- van der Hucht, K. A., Conti, P. S., Lundstrom, I., et al. 1981, *SSRv*, 28, 227. doi:10.1007/BF00173260
- van der Hucht, K. A., Williams, P. M., van Genderen, A. M., et al. 1989, *IAU Colloq. 113: Physics of Luminous Blue Variables*, 301. doi:10.1007/978-94-009-1031-7_51
- Walborn, N. R. 1973, *AJ*, 78, 1067. doi:10.1086/111509
- Walborn, N. R. 1977, *ApJ*, 215, 53. doi:10.1086/155334
- Williams, P. M., van der Hucht, K. A., & Thé, P. S. 1987, *A&A*, 182, 91
- Williams, P. M., Cohen, M., van der Hucht, K. A., et al. 1995, *MNRAS*, 275, 889. doi:10.1093/mnras/275.3.889